

Hexavalent chromium reduction by ZnO, SnO₂ and ZnO-SnO₂ synthesized using biosurfactants from extract of *Solanum macrocarpon*

Damian Onwudiwe (✉ Damian.Onwudiwe@nwu.ac.za)

North-West University (Mafikeng Campus)

Opeyemi Oyewo

Metallurgical and Materials Engineering, Tshwane University of Technology

Oluwasayo Esther Ogunjinmi

Department of Physical Sciences, First Technical University

Olusola Ojelere

University of Cologne Greinstraße 6

Original Research Full Papers

Keywords: ZnO, SnO₂, zinc tin oxide, complex metal oxides, green chemistry

Posted Date: February 1st, 2021

DOI: <https://doi.org/10.21203/rs.3.rs-160881/v1>

License: © ⓘ This work is licensed under a Creative Commons Attribution 4.0 International License.

[Read Full License](#)

Abstract

In this study, ZnO, SnO₂ and their composite (ZnO-SnO₂) were synthesized by green route using aqueous extract of *Solanum macrocarpon* fruit and were used for the photo-reduction of hexavalent chromium. The synthetic route involved a two-step procedure, induced by temperature via calcination at 350 and 600 °C. The composite was prepared by the treatment of a mixture of the precursor compounds to a temperature up to 800 °C, and the extension of the temperature to 1000 °C, resulted in the emergence of ZnO-SnO₂-ZTO. The nanoparticles were characterized by X-ray diffraction (XRD), transmission electron microscopy (TEM), and UV-vis spectroscopy. The XRD studies of the binary oxides confirmed a hexagonal wurtzite structure for the ZnO and a cubic structure for the SnO₂, without any change in the diffraction patterns or supplementary diffraction peaks. The morphology of the nanoparticles indicated fairly spherical shapes for the ZnO, that tend to agglomerate with increase in temperature. The SnO₂ showed rectangular shapes at both temperatures of reaction, while the ZnO-SnO₂ composite showed the presence of both morphologies of the component binary oxides. In the photo-enhanced degradation study, under ultra-violet light, the effect of pH (2–8), concentration of chromium(VI) (2–8 ppm), and photocatalyst dosage (25–150 mg/L) on the reduction of Cr(VI) to Cr(III) were investigated. The reduction showed higher efficiency in acidic environment than in the alkaline environment, and also with increase in photocatalyst dosage. The composite exhibited the highest photoreduction efficiency, above 90%, at the optimum condition of pH 2, 150 mg/L photocatalyst, 2 ppm chromium solution after 90 min. These low-cost and non-toxic metal oxide and their green synthesized composite have great potentials for Cr(VI) pollution clean-up from waste water.

1. Introduction

Chromium based materials are receiving considerable attention for their numerous applications such as in green pigments, heterogeneous catalysis, coating materials for thermal protection, and wear resistance. This is due to their excellent corrosion resistance, high hardness and good temperature-stability [1, 2]. However, the toxicity of chromium has been the main challenge hampering its potential applications. Chromium's toxicity has been reported to depend on its oxidation states, which ranges from + 6 to - 2; among which hexavalent chromium is the most toxic and second most stable oxidation state found in the environment [3, 4]. Hexavalent chromium poses severe threat to human health due to its high toxicity. Unlike organic pollutants, it is not biodegradable and could easily enter the food chain where it accumulates in living bodies over their life span [5, 6]. In the past few decades, there has been increasing effort to either remove Cr(VI) from the environment or reduce it to a less toxic Cr(III) with potential industrial applications. Consequently, several techniques have been employed for the removal of Cr(VI) ion from wastewater. Some of these methods include ion-exchange [7], electro reduction [8, 9], chemical reduction [10], biological reduction [11], and photocatalytic reduction [12]. Although, chemical routes have been reported to show maximum reduction rates compared to the other methods, it is however expensive and results in the generation of secondary waste, since it requires large amount of reducing agent [13,

14]. The photocatalytic reduction of pollutants from wastewater has been widely applauded as an efficient, cost effective and sustainable technology [15].

Recently, there has been an increased attention in the photocatalytic reduction of Cr(VI) to Cr(III) in wastewater treatment. This technology is based on the electron transfer on the surface of a semiconductor, when it is illuminated with light, resulting in the simultaneous redox reaction from photogenerated holes and electrons [16]. During this process, Cr(VI) could undergo photo-enhanced reduction to Cr(III) without the need for any reducing agent, which makes the approach a sustainable one [17]. Semiconductor nanoparticles are suitable for catalytic applications, as they possess high specific surface area with unique electronic correlation through spins and charge interactions. The broad usage of nanoparticles in environmental applications has resulted to an increased focus on the non-toxic materials which pose no potential hazard to the environment and may not adversely affect human health.

Zinc oxide (ZnO) and stannic oxide (SnO₂) are well known n-type, wide band gap metal oxides with band gap energies of ≈ 3.37 and 3.6 eV respectively in the UV region. They are both unique semiconducting materials that exhibits piezoelectric, and pyroelectric properties. Due to their wide bandgap energies, they are excellent candidates for optoelectronic materials and have versatile applications in sensors, piezoelectric devices, spin electronics, solar cells and anti-refractive coatings [18–21].

A number of different methods including physical and chemical routes have been devised for the synthesis of metal oxide nanoparticles, and SnO₂ and ZnO in particular. However, most of them employ the use of toxic chemicals [22, 23], involve longer reaction procedures and make use of sophisticated instrumentation [24]. The development of environmentally friendly methods for the synthesis of nanoparticles has recently generated high research interest in nanomaterials synthesis. This is due to the increasing awareness of green synthesis route and the need to obtain biologically compatible and environmentally benign materials. The biological routes seem to be in great focus as they serve as alternatives to chemical routes, and are not associated with the use of toxic reagents in the synthesis method [25, 26]. The three different templates used in the biosynthesis of nanomaterials includes enzymes, microorganisms and plant extracts[27]. The key reactions which are involved in biosynthesis of nanomaterials are reduction and oxidation processes. The synthesis procedure uses water as the solvent medium which is biocompatible and economical.

Solanum macrocarpon, commonly called garden egg, is a widespread plant genus of the family *Solanaceae*, mainly found in Asia and Tropical Africa. It is an edible crop and part of folklore remedy, which is used to curb elevated blood sugar, obesity, rheumatism, skin diseases, digestive difficulties, and some allergies [28, 29]. It contains appreciable amount of phytochemical and nutritive component including vitamins and minerals, which justify its therapeutic and nutritional applications. Some of its phytochemical contents includes high level of phenolic acids, flavonoids and anthocyanin with potent antioxidant activity, a potential beneficial action on hypercholesterolemia in humans [30, 31]. Apart from the medicinal values of *Solanum macrocarpon*, it could also be utilized in functionalizing nanomaterials for biomedical and environmental applications. In this study, the synthesis, optical and structural

properties of ZnO, SnO₂ nanoparticles and the composite (ZnO-SnO₂) using aqueous extract of *Solanum macrocarpon* was demonstrated and their photocatalytic reduction abilities towards chromium (VI) ion was investigated.

2. Materials And Methods

2.1 Preparation of the fruit extract

Solanum macrocarpon fruits were collected from Ekiti State, South Western region, Nigeria and were properly identified. The fruits were washed with distilled water to remove any dust, cut into pieces, air dried and pulverised. The aqueous extract was prepared by placing 25 g of the powder in 400 mL glass beaker containing 250 mL of distilled water. Thereafter, the mixture was boiled for 30 min to give a brown. The mixture was cooled to room temperature and filtered using Whatman No 1 filter paper, with pore size of 25 µm. The extract was stored in a refrigerator for further use [32].

2.2. Synthesis of SnO₂ and ZnO

About 50 mL aqueous solution of 0.1 M tin(IV) chloride pentahydrate [SnCl₄·5H₂O] was prepared. To this solution was added to 50 mL of the fruit extract in drop wise and stirred at 80°C for 2 h. The particles were collected by centrifuging the solution for 20 min. The product obtained were washed thoroughly with de-ionised water, again subjected to centrifugation for 20 min and then dried in hot air oven at 90°C overnight. Fine particles were obtained by grinding using mortar and pestle, and the powdered sample was calcined using muffle furnace at 350 and 600°C to get pure SnO₂ nanoparticles [33]. ZnO was prepared using similar procedure, but Zinc nitrate [Zn (NO₃)₂·6H₂O] was used as the precursor for Zn²⁺ ion.

2.3 Synthesis of ZnO-SnO₂ nanocomposite

The synthesis of the nanocomposite was carried out by firstly mixing 100 mL of 0.1 M zinc nitrate [Zn(NO₃)₂·6H₂O] with 50 mL of the fruit extract and of 1 M NaOH was added dropwise with vigorous stirring to adjust the pH to about 7. The solution was heated with continuous stirring for about 2 h, and thereafter 100 mL of 0.02 M tin(IV) chloride pentahydrate [SnCl₄·5H₂O] was added to the solution and heated at 80°C for another 2 h. Then, the solution was centrifuged, washed thoroughly with water and the product was dried in an oven at 90°C for 24 h [33]. The product was grounded, and the powdered fine particles were calcined using muffle furnace at 800°C for 1 h to get ZnO-SnO₂ nanocomposites.

2.4 Characterization of the nanoparticles

X-ray diffraction (XRD) analysis was carried using a Bruker-AXS D8 Advance diffractometer with CuK_α radiation operating at 40 kV and 30 mA for the determination of the crystal phase and composition of the nanoparticles. Absorption measurements were carried out using a Cary 300 UV-vis spectrophotometer. The particle sizes and morphology were analysed using a TECNAI G2 (ACI) transmission electron

microscope (TEM) operated at an accelerating voltage of 200, while the high-resolution TEM (HRTEM) was measured on JEM-2100 JEOL transmission electron microscopy.

2.5 Photocatalytic reduction of Cr(VI) to Cr(III)

In a typical photocatalytic experiments, 50 mL of the nanoparticles dispersion (1.0 g/L) containing 10 mg/L aqueous solution of Cr(VI) were stirred for about 30 min in the dark in order to establish the adsorption-desorption equilibrium [34]. In order to initiate the photocatalytic reaction, the solution was irradiated with a LED light (CEL-LED, 365 nm). The reduction of the Cr(VI) to Cr(III) was measured by analysing the concentration of Cr(VI) left in the solution by a UV spectrophotometer at the characteristic wavelength of 540 nm [35].

3. Results And Discussion

3.1 Synthesis of the nanoparticles

The phyto-components of the plant play a key role in the synthesis of the nanoparticles by acting as both reducing agents and surfactant, to influence the emergence of the nanoparticles. During the synthesis process, the reaction initiated via the complexation of the plant molecules to the metal ions and the formation of the respective hydroxides. The dehydration of the compounds and subsequent formation of the metal oxides is a thermal process and takes place via calcination. The temperature of the reaction influences both the size, morphology and crystallinity of the product. Routes (i), (ii) and (iii) in Figure 1 presents the synthesis process for the formation of the ZnO, SnO₂ and the composites respectively.

3.2. Structural characterization

The XRD patterns of the ZnO and SnO₂ samples at two different calcination temperatures are shown in Figures 1 and 2 respectively. The diffraction peaks of ZnO after 1 h calcination at 350 and 600 °C are presented in Figures 2 a and b. In both samples, the peaks which appeared around 32, 34, 36, 48, 57, 63, 68 and 69° are respectively ascribed to the 100, 002, 101, 102, 110, 103, 112 and 201 crystallographic planes. These indices matched with the JCPDS file number 36–1451 [36]. In the SnO₂ samples calcined at 350 and 600 °C, and presented in Figures 3 a and b, the diffraction peaks around 27, 32, 38, 53, 57, and 66 were attributed respectively to 110, 101, 200, 211, 002, and 112 facets of tetragonal SnO₂ which matched well with JCPDS file number 41–1445 [37].

The diffraction patterns of both ZnO and SnO₂ after 1 hr, at different calcination temperatures, showed no prominent differences as both samples showed the same phases and peak positions. However, it could be observed that as the calcination time was increased, a prominent increase in the intensity of the peaks also occurred. The average sizes of the ZnO particles were calculated by the Scherer formula and found to be 64 and 82 nm. The Scherer approach to particle size estimation was not applied to the SnO₂ due to the anisotropic morphology.

Figure 4 presents the XRD of the complex metal oxide nanoparticles. The presence of the XRD peaks of both ZnO and SnO₂ confirmed the successful formation of heterojunction between the two metal oxides. Interestingly and contrary to the observation in the binary oxides, as the calcination temperature was increased to 800 °C, the intensity of the peaks decreased with increased sharpness but no observable phase change occurred. This was indicative of some increase in the particles' size. Furthermore, as the calcination temperature increased to 1000 °C, a new intermediate phase appeared. In Figure 4b, the diffraction peaks at 17.83, 29.12, 34.33, 41.53, 55.08, 60.43, 71.51, and 71.62 were indexed to (111), (220), (311), (400), (511), (440), (533), and (622), which matched well with JCPDS file no 24-1470 and were assigned to zinc stannate (Zn₂SnO₄) with a cubic geometry[38]. Similar observation has been reported by Ali *et al.* [39].

3.3 Morphology

The TEM images, presented in Figure 5, revealed that the ZnO samples consisted of aggregates of particles with fairly spherical morphology, and average sizes that appeared quite close for the samples obtained at 650 °C (Fig 5b) compared to the samples obtained at 350 °C (Fig. 5a). As shown in Fig. 6a, the SnO₂ particles had a rectangular shape, which remained unchanged even after calcination at 650 °C (Fig 6b), although with observable size increase. The micrographs of the mixed metal oxide ZnO–SnO₂ presented in Fig. 7a revealed high agglomeration, perhaps due to the high temperature and increase in surface reactivity. The mixing of two different oxides have been reported to generally result in limiting the growth of both oxides in the system. As could be observed in the micrograph, the mean sizes of the individual metal oxides, ZnO and SnO₂, presented in Figures 5 and 6 were larger than in the mixed metal oxides ZnO–SnO₂ (Fig. 7). The mixing of both oxides resulted in the reduction of the crystallite size of the mixed oxides, and this was consistent with previous reports on mixed metal oxides of ZnO and SnO₂ [40, 41]. Although, the presence of both morphologies of the component binary oxides were still observable, the high degree of agglomeration impeded the correct estimation of particles size.

Figure 7b is a representative TEM images of ZnO-SnO₂-ZTO. The high-resolution TEM image in the inset of Figure 7b evidenced the presence of overlapped images rather than images that grew from a common spot to form star shaped morphology. It also evidenced the intergrown lattices of the different metal oxides.

3.4 Absorption spectra

Figures 8 and 9 present the absorption spectra of the prepared ZnO and SnO₂ nanoparticles respectively, obtained after 1 h at different temperatures (a and b). In both cases, the samples showed absorption peaks in the UV region. In semiconductor nanoparticles whose dimensions falls within the order of their bulk excitation, some unique optical properties are exhibited and these are strongly dependent on the size [42]. In the ZnO nanoparticles, sharp increase in the absorption around 330 nm was observed. This feature in the optical spectrum, which occurred around 300 nm in the spectra of the SnO₂ nanoparticles, is related to the transition between the valence band and the conduction band [43], and is known as the

optical absorption edge. The optical band gap (E_g) energies of the nanoparticles were calculated using the Tauc's relation $\{\alpha = A(h\nu - E_g)^{0.5}\}$; where A is a constant, α is the optical absorption and $h\nu$ is photon energy [44]. The band gap energy E_g of the nanoparticles could be obtained by extrapolating the zero absorption coefficient determined from the Tauc relation. In these direct band gap materials, the intercept of the tangent to the plot gave a good estimation of their band gap energies (as shown in the inset of Figures 8 and 9). The optical direct band gap energies (E_g) of the prepared samples were calculated to be 3.75 and 3.62 for ZnO obtained for the product at 350 and 600 °C respectively. In the SnO₂, the obtained values were 4.20 and 4.05 eV respectively.

Optical band gap decreases with increase in particle size, and this result in a concomitant shift in the absorption edge to a lower energy. The absorption edge in the spectra of ZnO and SnO₂ nanoparticles calcined at 350 and 600 °C showed a red shift at both temperatures. This shift in the absorption onset is characteristic of particle growth. The band gap energies of the synthesized nanoparticles were larger than their respective bulk values of 3.62 and 3.34 eV for SnO₂ and ZnO respectively [45, 46]. The reduction in the band gap values after longer calcination time may be ascribed to the enhanced surface reactivity in the samples during calcination, which resulted into particles growth and higher degree of agglomeration observed in the products. A gradual shift towards macrocrystalline materials with increase in reaction temperature may be proposed, hence the observed shift in the absorption onset.

3.5 Photocatalyst reduction of Cr(VI) to Cr(III)

Hexavalent chromium could exist in three different ionic forms, including hydro chromate, chromate and dichromate, with the following ionic formula: (HCrO_4^-), (CrO_4^{2-}), and ($\text{Cr}_2\text{O}_7^{2-}$) respectively. Although the chromate ion is reported to predominate in both neutral and basic media, solutions of lower pHs favours the hydrochromium and this indicates the pH dependence of the different species [47].

The amount of Cr(VI) remaining at any given time was calculated using the relationship:

$$[\text{Cr}_{(\text{Tot})}] - [\text{Cr}(\text{VI})] = [\text{Cr}(\text{III})],$$

$$\frac{[\text{Cr}_{(\text{Tot})}] - [\text{Cr}(\text{VI})]}{[\text{Cr}_{(\text{Tot})}]}$$

3.5.1 Effects of solution pH

The pH of a solution is crucial in any water treatment process involving the removal of metal ions from water. This is because the chemistry of the metal ions in aqueous solution is mostly influenced by any change in pH and often significantly affect the performance of materials used in water remediation from pollutants. Therefore, it is imperative to investigate the effect of solution pH prior to other process

variables. In order to determine the optimal pH, a solution of Cr(VI) with initial concentration of 2 ppm and 100 mg/L dosage of each synthesized catalysts was prepared and the solution pH was varied from 2 to 8, as presented in Fig.10 (a-c). Similar trend could be observed in the performance of all the synthesized catalysts used in the study, with a maximum reduction of Cr (VI) at the solution pH of 2. Since Cr(VI) is present as $\text{Cr}_2\text{O}_7^{2-}$, HCrO_4^- and CrO_4^{2-} in aqueous media with an overall negative charge [48], the highest reduction of Cr(VI) at the lowest studied pH values may be due to the development of an overall positive charges on the surface of the catalysts. Consequently, this process would result in the electrostatic attraction of the negatively charged chromium ions. The reduction in the removal of the dichromate ion at higher pH might be associated with the effect of the negatively charged catalysts, which repels the negatively charged chromium ions. Although, the optimum Cr(VI) reduction was observed at pH of 2 in all cases, the nanocomposite catalyst is observed to be more beneficial, perhaps due to the good separation of photogenerated charges, the formation of heterojunction and delayed recombination of photoelectron-hole (Fig. 10c) compared to ZnO and SnO₂ nanoparticles[49, 50]. Consequently, nanocomposite catalysts was used for the subsequent photocatalysis experiments in this study [51]. The synergetic effect of the two binary semiconductors coexisting in the ZnO/SnO₂ heterojunction, in addition to the small size of the nanocomposite are important factors that are responsible for the observed increased efficiency.

3.5.2 Effect of catalyst loading on Cr(VI) photo reduction

The optimal pH of 2 was selected in order to study the effect of change in the nanocomposite loading with predetermined initial Cr(VI) concentration of 2 ppm [17]. There was considerable increase in the total conversion of Cr(VI) to Cr(III) as the catalysts loading increased from 25 mg/L to 100 mg/L as presented in Fig. 11. This could be attributed to the enhancement in the total surface area with increase in dosage of catalyst, which provided more active sites for interaction with the chromium ions. An initial decrease in the reduction of Cr(VI) could be noticed at the onset, above 100 mg/L catalysts loading, which is an indication that the optimum catalyst loading for 2 ppm is around 100 mg/L [52]. Therefore, the decrease in Cr(VI) conversion to Cr(III) at 125 and 150 mg/L of catalyst loading was an indication that the dosage was superfluously based on this operating condition[53, 54].

3.5.3 Effect of the initial concentration of Cr(VI) on the removal efficiency of ZnO-SnO₂ nanocomposite

The conversion of Cr(VI) to Cr(III) using different initial concentration of the Cr(VI) was investigated at the optimal pH 2 and dosage of 100 mg/L. The result, presented in Figure 12, showed that the higher the concentration of the Cr(VI) in the solution, the lower the photocatalytic conversion of Cr(VI) to Cr(III). At 8 ppm, only about 0.5 of the initial concentration of the Cr(VI) was totally converted, which was only 50% of the initial concentration of the Cr(VI) in the solution. This could be because at higher concentration of the Cr(VI), the product of the conversion process, Cr(III), could not be quickly separated from the surface of the catalyst. This would, therefore, result in the covering of the active sites of the photocatalyst, thereby causing the lowering of the photocatalytic activity [55]. The results obtained in all the studies involving investigating the effect of the initial concentration of Cr(VI) were consistent. This is an indication that the rapid separation of Cr(III) from the catalyst surface is an important factor in the improvement of the

activity and stability of photocatalytic reduction of hexavalent chromium [56]. In this study, the initial concentration of 2 ppm yielded the optimum conversion of Cr(VI) to Cr(III).)

3.6 Photocatalytic mechanism

Figure 13 presents the schematic diagram of the band structure and photogenerated electron–hole (e^- – h^+) separation in the ZnO-SnO₂ composite. As illustrated in the diagram, the strong combination of the two metal oxides to form nanocomposite had improved activity in the reduction of chromium(VI) to chromium(III). The coupling of two semiconductor nanomaterials with different band gap energies has been demonstrated as one of the effective ways of decreasing the rate of recombination of electron-hole (e^-/h^+) pairs [57, 58].

Both ZnO and SnO₂ absorb in the UV region of the electromagnetic spectrum as a result of their wide band gap energies. The two metal oxides possess suitable electronic properties and are coupled for improved performance. The conduction band potential of ZnO is -0.36 eV, which is lower than that of SnO₂ (-0.11 eV), while the valence band potential of SnO₂ is $+3.44$ eV and is higher than that of ZnO ($+2.84$ eV) (Figure 13 a) [57]. Upon the irradiation of the composite by UV light, Figure 13b, the photogenerated electrons with negative charges migrate from the low potential to high potential energy. At the same time, the positive holes migrate in the opposite direction. This implies that the electrons migrate from the conduction band of the ZnO to the conduction band of the SnO₂, whereas the holes migrate from the valence band of SnO₂ to the valence band of the ZnO [59]. Consequently, in the conduction band of SnO₂ is the accumulation of photogenerated electrons, while in the valence band of ZnO is the accumulation of holes. The formation of a junction results in the separation of the electrons and holes that highly restrained the recombination process and effective electron–hole separation is therefore accomplished on the surface of photocatalyst. As a result, more electrons participate in the photoreduction for the effective conversion of Cr(VI) to Cr(III) by the composite semiconductor. This was responsible for the marked enhancement in the photocatalytic activity of ZnO-SnO₂ composite relative to that of pure ZnO and SnO₂.

Conclusion

In a two-step procedure, using aqueous extract of *Solanum macrocarpon* fruit, ZnO, SnO₂ and ZnO-SnO₂ nanoparticles (NPs) were successfully prepared. The biomolecules present in the fruit's extract acted as capping as well as complexing agents to form the respective metal hydroxides. The calcination of the metal hydroxides resulted in the thermal transformation to their respective oxides. Subsequent treatment of a mixture of the precursor compounds to a temperature up to 800 °C led to the formation of complex metal oxide, ZnO-SnO₂, with the formation of a new intermediate phase of zinc stannate (Zn₂SnO₄) appearing at 1000 °C. A photoreduction of hexavalent chromium to the trivalent specie was evaluated at different solution pH, initial chromium concentration and photocatalyst dosage. The photoreduction efficiency of the nanocomposite showed superior performance compared to the binary oxides, ZnO and

SnO₂. The higher reduction efficiency of the nanocomposite could be ascribed to the improved charge separation and suppressed electron-hole pairs recombination process, which was achieved by the coupling of ZnO and SnO₂. This method offers an environmental friendly approach to binary oxides and their complex metal oxides, which could also be extended to other metal oxides.

Declarations

Acknowledgement

DCO acknowledges funding of this work by National Research Foundation (NRF) South Africa and North-West University, South Africa.

References

- [1] M. Abecassis-Wolfovich, H. Rotter, M.V. Landau, E. Korin, A.I. Erenburg, D. Mogilyansky, E. Garshtein, Texture of chromia aerogels and structure of their nanocrystals, in: S.-E. Park, R. Ryoo, W.-S. Ahn, C.W. Lee, J.-S. Chang (Eds.) *Studies in Surface Science and Catalysis*, Elsevier. 247-250 (2003) .
- [2] E. Sourty, J.L. Sullivan, M.D. Bijker, Chromium oxide coatings applied to magnetic tape heads for improved wear resistance., *Tribology International*. **36**, 389-396 (2003).
- [3] A. Ertani, A. Mietto, M. Borin, S. Nardi, Chromium in Agricultural Soils and Crops: A Review, *Water, Air, & Soil Pollution*. **228**, 190 (2017).
- [4] V. Velma, S.S. Vutukuru, P.B. Tchounwou, Ecotoxicology of hexavalent chromium in freshwater fish: a critical review, *Rev Environ Health*. **24**, 129-145 (2009) .
- [5] P.B. Tchounwou, C.G. Yedjou, A.K. Patlolla, D.J. Sutton, Heavy metal toxicity and the environment, *Exp Suppl*. **101**, 133-164 (2012).
- [6] M. Jaishankar, T. Tseten, N. Anbalagan, B.B. Mathew, K.N. Beeregowda, Toxicity, mechanism and health effects of some heavy metals, *Interdiscip Toxicol*. **7**, 60-72 (2014).
- [7] L.-L. Li, X.-Q. Feng, R.-P. Han, S.-Q. Zang, G. Yang, Cr(VI) removal via anion exchange on a silver-triazolate MOF, *Journal of hazardous materials*. **321**, 622-628 (2017).
- [8] H. Peng, Y. Leng, Q. Cheng, Q. Shang, J. Shu, J. Guo, Efficient Removal of Hexavalent chromium from Wastewater with Electro-reduction. , *Processes*. **7**, 41 (2019).
- [9] A.K. Golder, A.K. Chanda, A.N. Samanta, S. Ray, Removal of hexavalent chromium by electrochemical reduction–precipitation: Investigation of process performance and reaction stoichiometry, *Separation and Purification Technology*. **76**, 345-350 (2011).

- [10] Y. Zhu, H. Li, G. Zhang, F. Meng, L. Li, S. Wu, Removal of hexavalent chromium from aqueous solution by different surface-modified biochars: Acid washing, nanoscale zero-valent iron and ferric iron loading, *Bioresour Technol.* **261**, 142-150 (2018).
- [11] A. Demir, M. Arisoy, Biological and chemical removal of Cr(VI) from waste water: cost and benefit analysis, *J Hazard Mater.* **147**, 275-280 (2007).
- [12] X. Wang, S.O. Pehkonen, A.K. Ray, Removal of Aqueous Cr(VI) by a Combination of Photocatalytic Reduction and Coprecipitation, *Industrial & Engineering Chemistry Research.* **43**, 1665-1672 (2004).
- [13] H.W. Ma, J.F. Shen, M. Shi, X. Lu, Z.Q. Li, Y. Long, N. Li, M.X. Ye, Significant enhanced performance for Rhodamine B, phenol and Cr(VI) removal by Bi₂WO₆ nanocomposites via reduced graphene oxide modification, *Applied Catalysis B: Environmental.* **121**, 198-205 (2012).
- [14] A. Pandikumar, R. Ramaraj, Titanium dioxide-gold nanocomposite materials embedded in silicate sol-gel film catalyst for simultaneous photodegradation of hexavalent chromium and methylene blue, *Journal of hazardous materials.* **203-204**, 244-250 (2012).
- [15] R. Acharya, B. Naik, K. Parida, Cr(VI) remediation from aqueous environment through modified-TiO₂-mediated photocatalytic reduction, *Beilstein journal of nanotechnology.* **9** 1448-1470 (2018).
- [16] A. Fujishima, X. Zhang, D.A. Tryk, TiO₂ photocatalysis and related surface phenomena, *Surface Science Reports.* **63**, 515 (2008).
- [17] D.C. Onwudiwe, O.A. Oyewo, U. Atamtürk, O. Ojelere, S. Mathur, Photocatalytic reduction of Cr(VI) using star-shaped Bi₂S₃ obtained from microwave irradiation of bismuth complex, *Journal of Environmental Chemical Engineering.* **8**, 103816 (2020).
- [18] F. Gu, S.F. Wang, M.K. Lu, G.J. Zhou, D. Xu, D.R. Yuan, Photoluminescence properties of SnO₂ nanoparticles synthesized by sol-gel method, *J. Phys. Chem. B.* **108**, 8119-8812 (2004).
- [19] T.L. Villarreal, G. Boschloo, Hagfeldt., Nanostructured zinc stannate as semiconductor working electrodes for dye-sensitized solar cells, *J. Phys. Chem. C.* **111**, 5549-5556 (2007).
- [20] Z.L. Wang, Nanostructures of zinc oxide, *Mater Today.* **7**, 26–33 (2004) .
- [21] R. Wahab, Y.S. Kim, D.S. Lee, J.M. Seo, H.S. Shin, Controlled synthesis of zinc oxide nanoneedles and their transformation to microflowers, *Sci Adv Mater.* **2**, 424–435 (2010).
- [22] H.J. Zhai, W.H. Wu, F. Lu, H.S. Wang, Effects of ammonia and CTAB on morphologies of ZnO nano- and micromaterials under solvothermal process, *Mater Chem Phys.* **112**, 1024–1028 (2008).
- [23] R. Noonuruk, N. Vittayakorn, W. Mekprasart, J. Sritharathikhun, W. Pecharapa, *Journal of Nanoscience and Nanotechnology.* **15**, 2564 (2015) .

- [24] S.K. Tammina, B.K. Mandal, N.K. Kadiyala, Photocatalytic degradation of methylene blue dye by nonconventional synthesized SnO₂ nanoparticles. *10* (2018) *Environmental Nanotechnology, Monitoring & Management* **10**, 339-350 (2018).
- [25] X. Fuku, K. Kaviyarasu, N. Matinise, M. Maaza, Punicalagin green functionalized Cu/Cu₂O/ZnO/CuO nanocomposite for potential electrochemical transducer and catalyst, *Nanoscale Res. Lett.* **11**, 9-14 (2016).
- [26] C.M. Magdalane, K. Kaviyarasu, J.J. Vijaya, C. Jayakumar, M. Maaza, B. Jeyaraj, Photocatalytic degradation effect of malachite green and catalytic hydrogenation by UV-illuminated CeO₂/CdO multilayered nanoplatelet arrays: investigation of antifungal and antimicrobial activities, *J. Photochem. Photobiol. B Biol.* **169**, 110-123 (2017) .
- [27] J. Hu, Biosynthesis of SnO₂ nanoparticles by fig (*Ficus carica*) leaf extract for electrochemically determining Hg(II) in water samples, *Int. J. Electrochem. Sci.* **10**, 10668-10676 (2015).
- [28] P.M.L. Jaeger, F.N. Hepper, A review of the genus *Solanum* in Africa, In: *Solanaceae, biology and systematics*. 41–55 (1986).
- [29] K.O. Bonsu, D.A. Fontem, G.O. Nkansah, I.R. N., E.O. Owusu, R.R. Schippers, Diversity within the Gboma eggplant (*Solanum macrocarpon*), an indigenous vegetable from West Africa., *Ghana J. Horticulture.* **1**, 50–58 (2002).
- [30] G. Niño-Medina, Structure and content of phenolics in eggplant (*Solanum melongena*) - a review, *South African journal of botany.* **111**,161-169 (2017).
- [31] A. Djouadi, T. Lanez, C. Boubekri, . Evaluation of antioxidant activity and polyphenolic contents of two South Algerian eggplants cultivars., *J. Fundam. Applied Sci.* **8**, 223-231 (2016).
- [32] R. Yuvakkumar, J. Suresh, A.J. Nathanael, M. Sundrarajan, S.I. Hong, Novel green synthetic strategy to prepare ZnO nanocrystals using rambutan (*Nephelium lappaceum* L.) peel extract and its antibacterial applications, *Materials science & engineering. C, Materials for biological applications.* **41**, 17-27 (2014) .
- [33] E.E. Elemike, D.C. Onwudiwe, M. Singh, Eco-friendly Synthesis of Copper Oxide, Zinc Oxide and Copper Oxide–Zinc Oxide Nanocomposites, and Their Anticancer Applications, *Journal of Inorganic and Organometallic Polymers and Materials.* **30**, 400-409 (2020).
- [34] Z. Bian, T. Tachikawa, T. Majima, Superstructure of TiO₂ crystalline nanoparticles yields effective conduction path ways for photogenerated charges, *J. Phys. Chem. Lett.* **3**, 1422–1427 (2012).
- [35] X. Yuan, Y. Wang, J. Wang, C. Zhou, Q. Tang, X. Rao, Calcined graphene/MgAl-layered double hydroxides for enhanced Cr(VI) removal, *Chem. Eng. J.* **221**, 204–213 (2013).

- [36] L.F. da Silva, J.C. M'Peko, A.C. Catto, S. Bernardini, V.R. Mastelaro, K. Aguir, C. Ribeiro, E. Longo, UV-enhanced ozone gas sensing response of ZnO-SnO₂ heterojunctions at room temperature, *Sensors and Actuators B: Chemical*. **240**, 573-579 (2017).
- [37] P. Pascariu, A. Airinei, N. Olaru, L. Olaru, V. Nica, Photocatalytic degradation of Rhodamine B dye using ZnO-SnO₂ electrospun ceramic nanofibers *Ceram. Int.* **42**, 6775-6781 (2016).
- [38] Y. Li, N. Luo, G. Sun, B. Zhang, L. Lin, H. Jin, Y. Wang, H. Bala, J. Cao, Z. Zhang, In situ decoration of Zn₂SnO₄ nanoparticles on reduced graphene oxide for high performance ethanol sensor, *Ceramics International*. **44**, 6836-6842 (2018).
- [39] W. Ali, H. Ullah, A. Zada, M.K. Alamgir, W. Muhammad, M.J. Ahmad, A. Nadhman, Effect of calcination temperature on the photoactivities of ZnO/SnO₂ nanocomposites for the degradation of methyl orange, *Materials Chemistry and Physics*. **213**, 259-266 (2018).
- [40] C. Wang, J. Zhao, X. Wang, B. Mai, G. Sheng, P. Peng, J. Fu, *Appl. Catal. B: Environ.*, **39**, 269–279 (2002).
- [41] C. Wang, X. Wang, B. Xu, J. Zhao, B. Mai, P. Peng, G. Sheng, J. Fu, *Photochem. Photobiol. A: Chem.* **168**, 47–52 (2004).
- [42] F. Gu, S.F. Wang, M.K. Lü, G.J. Zhou, D. Xu, D.R. Yuan, Photoluminescence Properties of SnO₂ Nanoparticles Synthesized by Sol–Gel Method, *The Journal of Physical Chemistry B*. **108**, 8119-8123 (2004).
- [43] H. Mahdhi, Z.B. Ayadi, J.L. Gauffier, K. Djessas, S. Alaya, Effect of sputtering power on the electrical and optical properties of Ca-doped ZnO thin films sputtered from nanopowders compacted target., *Opt. Mater.* **45**, 97-103 (2015).
- [44] S.G. Alamdari, M.S. Ghamsari, M.J. Tafreshi, Synthesis , Characterization , and Gas Sensing Properties of In-doped ZnO, in, (2018).
- [45] M. Karmaoui, A.B. Jorge, P.F. McMillan, A.E. Aliev, R.C. Pullar, J.A. Labrincha, D.M. Tobaldi, One-Step Synthesis, Structure, and Band Gap Properties of SnO₂ Nanoparticles Made by a Low Temperature Nonaqueous Sol–Gel Technique, *ACS Omega*. **3**, 13227-13238 (2018).
- [46] H. Mahdhi, S. Alaya, J.L. Gauffier, K. Djessas, B.A. Z., Influence of thickness on the structural, optical and electrical properties of Ga-doped ZnO thin films deposited by sputtering magnetron., *J. Alloy. Comp.* **695**, 697-703 (2017).
- [47] F. Zewdu, M. Amare, Determination of the level of hexavalent, trivalent, and total chromium in the discharged effluent of Bahir Dar tannery using ICP-OES and UV–Visible spectrometry, *Cogent Chemistry*. **4**, 1534566 (2018).

- [48] H. Wang, S. Zhang, J. Wang, Q. Song, W. Zhang, Q. He, J. Song, F. Ma, Comparison of performance and microbial communities in a bioelectrochemical system for simultaneous denitrification and chromium removal: Effects of pH, *Process Biochemistry*. **73**, 154-161 (2018).
- [49] Q. Zhang, X. Zhao, L. Duan, H. Shen, R. Liu, Controlling oxygen vacancies and enhanced visible light photocatalysis of CeO₂/ZnO nanocomposites, *Journal of Photochemistry and Photobiology A: Chemistry*. **392**, 112156 (2020).
- [50] E. Irani, M. Amoli-Diva, Hybrid adsorption–photocatalysis properties of quaternary magneto-plasmonic ZnO/MWCNTs nanocomposite for applying synergistic photocatalytic removal and membrane filtration in industrial wastewater treatment, *Journal of Photochemistry and Photobiology A: Chemistry*. **391**, 112359 (2020).
- [51] R. Aggarwal, G. Arora, Assessment of biosorbents for chromium removal from aqueous media, *Materials Today: Proceedings*, (2020).
- [52] V. Kumar, S.K. Dwivedi, Hexavalent chromium reduction ability and bioremediation potential of *Aspergillus flavus* CR500 isolated from electroplating wastewater, *Chemosphere*. **237**, 124567 (2019).
- [53] S. Ding, A. Li, S. Jiang, Y. Zhou, Q. Wei, W. Zhou, Y. Huang, Q. Yang, T. Fan, Niobium modification effects on hydrodesulfurization of 4,6-DMDBT catalyzed on Ni-Mo-S active sites: A combination of experiments and theoretical study, *Fuel*. **237**, 429-441 (2019).
- [54] D. Gavril, A. Georgaka, V. Loukopoulos, G. Karaiskakis, Inverse gas chromatographic investigation of the active sites related to CO adsorption over Rh/SiO₂ catalysts in excess of hydrogen, *Journal of Chromatography A*. **1160**, 289-298 (2007).
- [55] S. Rafiaee, M.R. Samani, D. Toghraie, Removal of hexavalent chromium from aqueous media using pomegranate peels modified by polymeric coatings: Effects of various composite synthesis parameters, *Synthetic Metals*. **265**, 116416 (2020).
- [56] X. Deng, Y. Chen, J. Wen, Y. Xu, J. Zhu, Z. Bian, Polyaniline-TiO₂ composite photocatalysts for light-driven hexavalent chromium ions reduction, *Science Bulletin*. **65**, 105-112 (2020).
- [57] Z. Khodami, A. Nezamzadeh-Ejhieh, Investigation of photocatalytic effect of ZnO-SnO₂/nano clinoptilolite system in the photodegradation of aqueous mixture of 4-methylbenzoic acid/2-chloro-5-nitrobenzoic acid, *J. Mol. Catal. A: Chem.* **409**, 59-68 (2015).
- [58] J. Lin, Z. Luo, J. Liu, P. Li, Photocatalytic degradation of methylene blue in aqueous solution by using ZnO-SnO₂ nanocomposites, *Materials Science in Semiconductor Processing*, **87**, 24-31 (2018).
- [59] Z. Chen, H. Gong, Q. Liu, M. Song, C. Huang, NiSe₂ nanoparticles grown in situ on CdS nanorods for enhanced photocatalytic hydrogen evolution., *ACS Sustain. Chem. Eng.* **7**, 16720-16728 (2019).

Figures

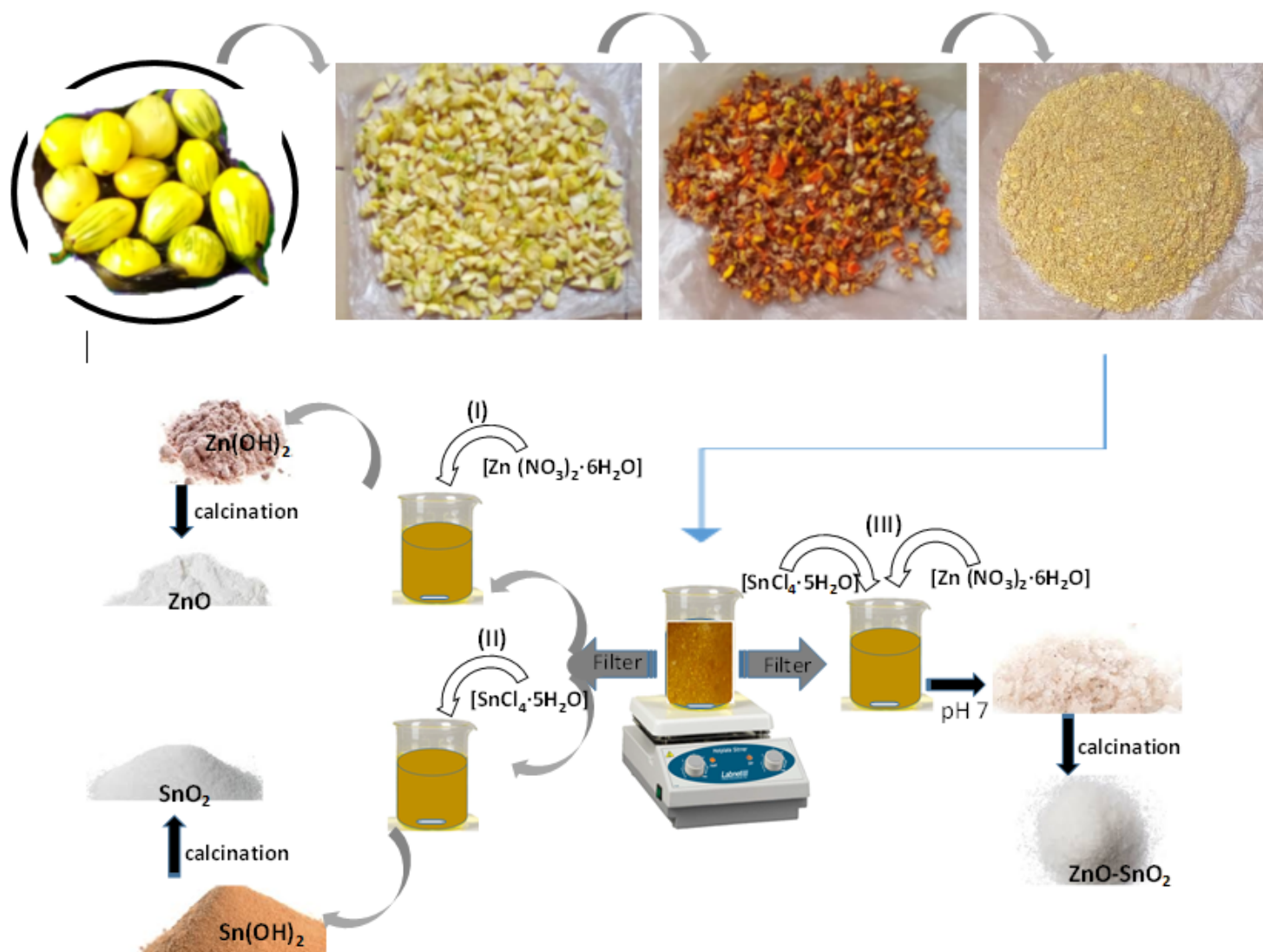


Figure 1

Synthetic route for the formation of ZnO, SnO₂ and the composites (ZnO-SnO₂) using aqueous extract of Solanum macrocarpon.

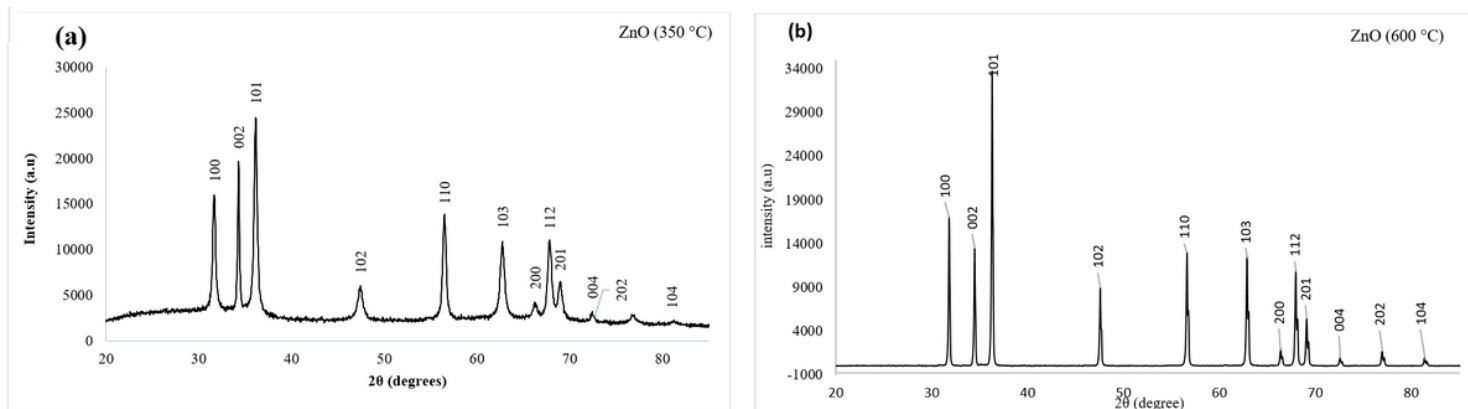


Figure 2

XRD patterns of ZnO calcined at (a) 350 C and (b) 600 C for 1 h

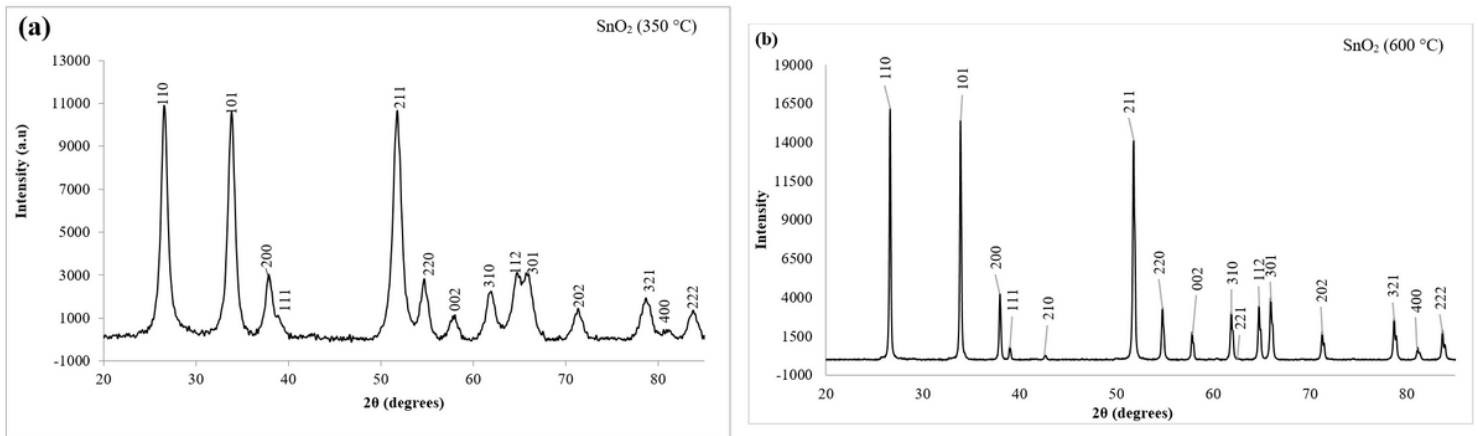


Figure 3

XRD patterns of SnO₂ calcined at (a) 350 °C and (b) 600 °C for 1 h

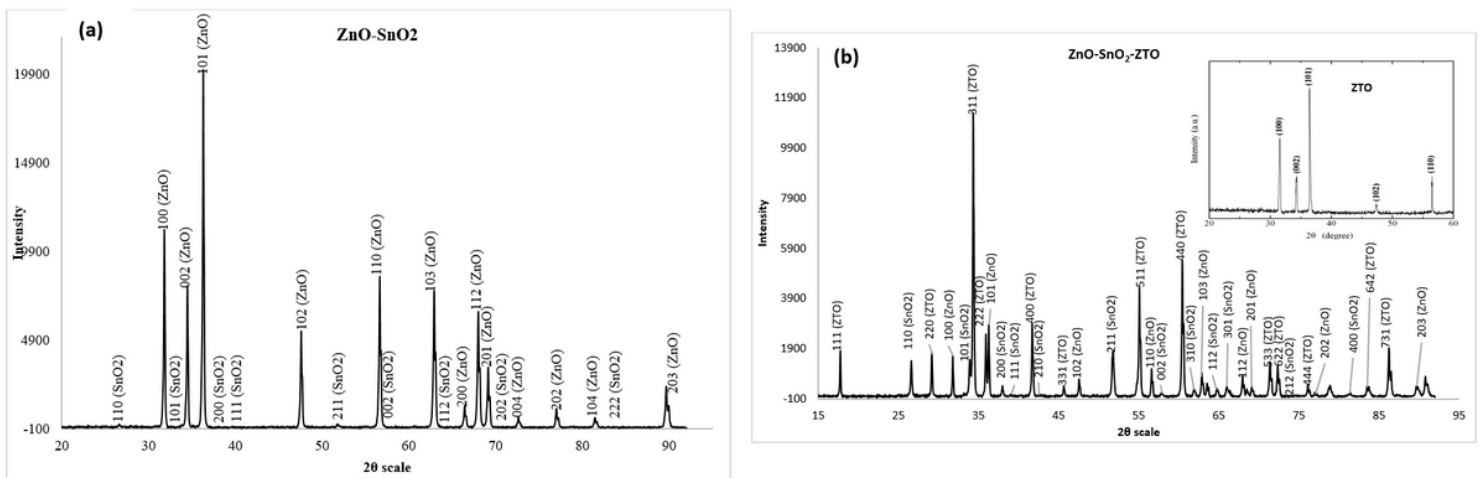


Figure 4

XRD patterns of (a) ZnO-SnO₂, and (b) ZnO-SnO₂-ZTO nanoparticles synthesized by calcination at 800 and 1000 °C respectively.

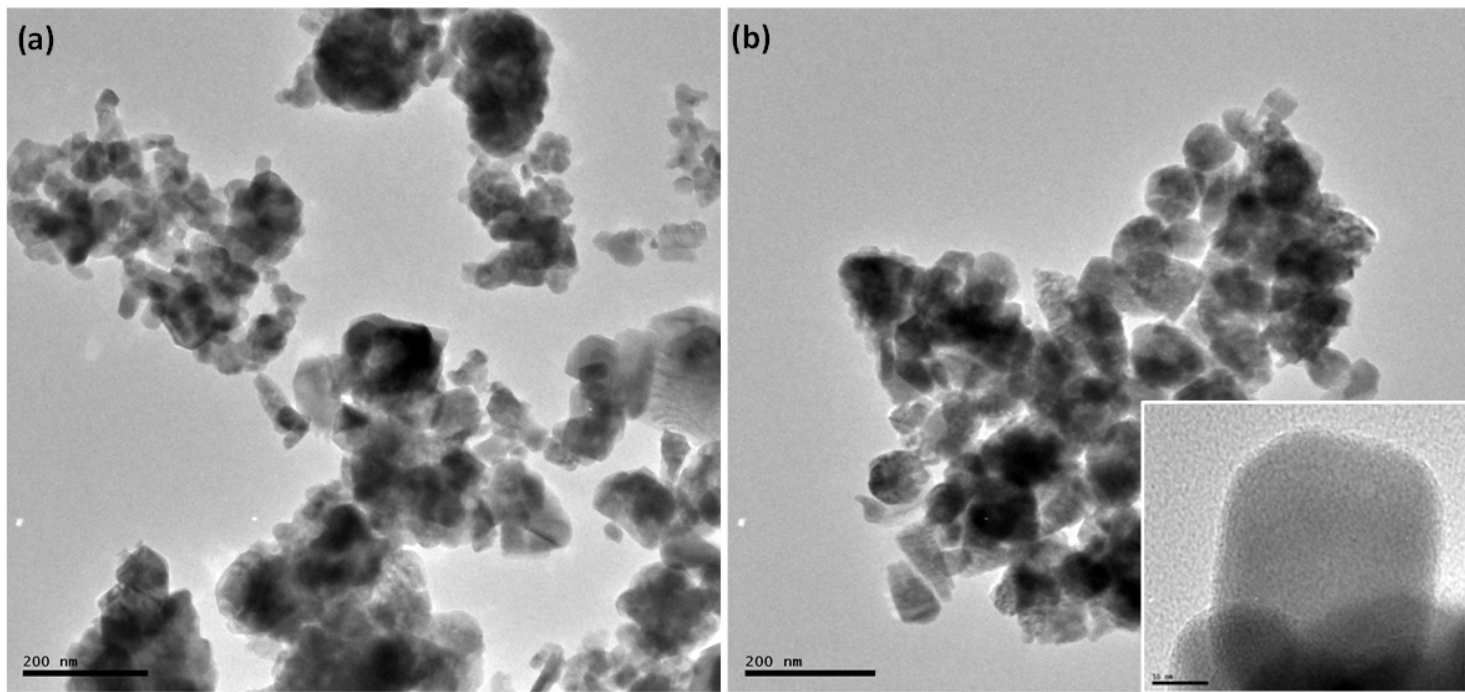


Figure 5

TEM images of ZnO calcined at (a) 350 °C and (b) 600 °C for 1 h (inset is the HRTEM).

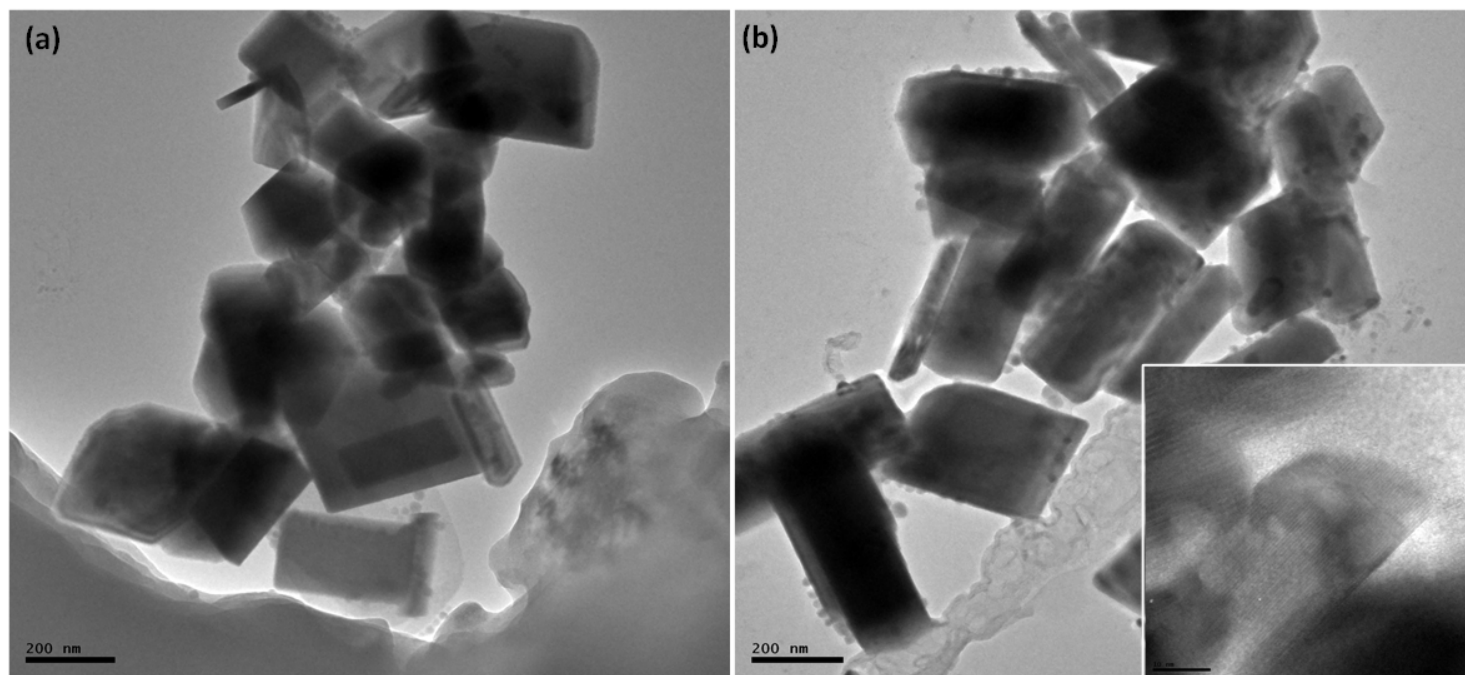


Figure 6

TEM images of SnO₂ calcined at (a) 350 °C and (b) 600 °C for 1 h (inset is the HRTEM).

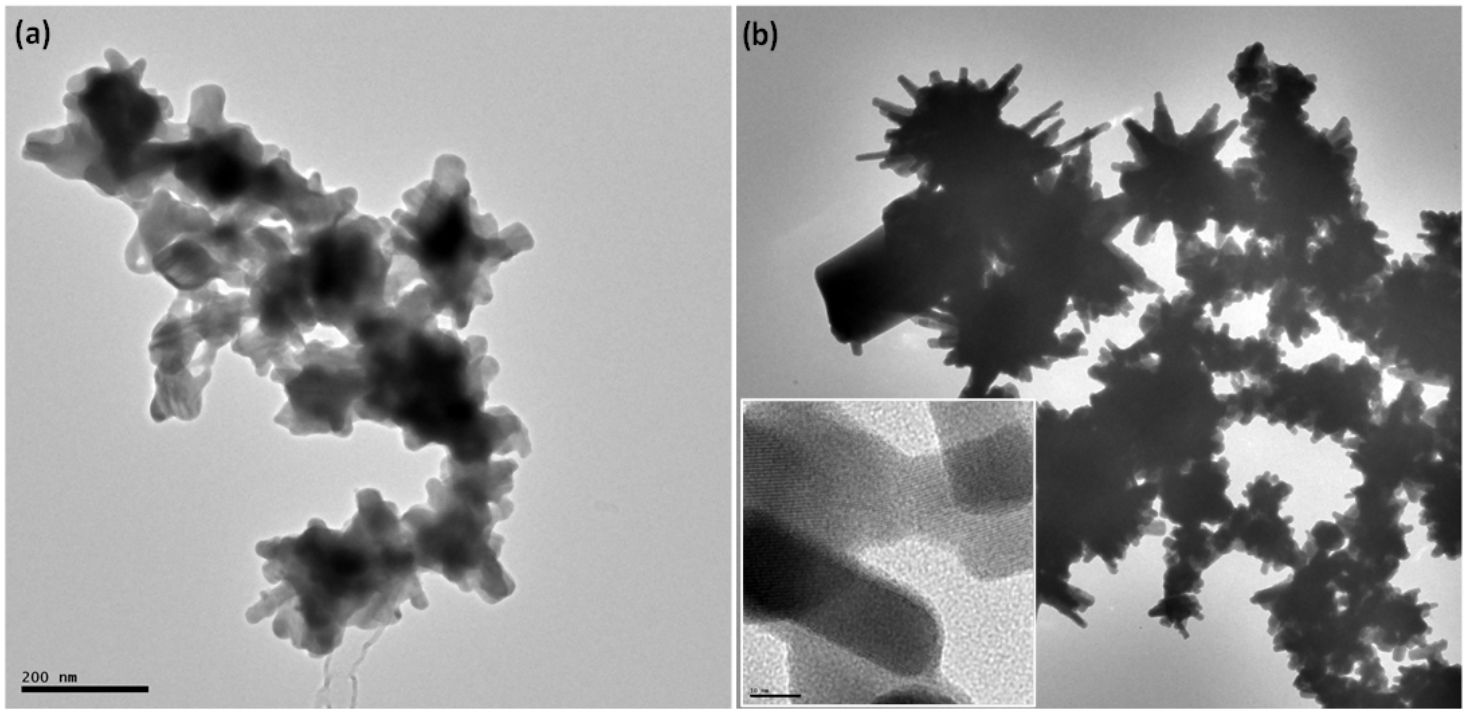


Figure 7

TEM images of (a) ZnO-SnO₂, and (b) ZnO-SnO₂-ZTO nanoparticles synthesized by calcination after 800 and 1000 °C respectively.

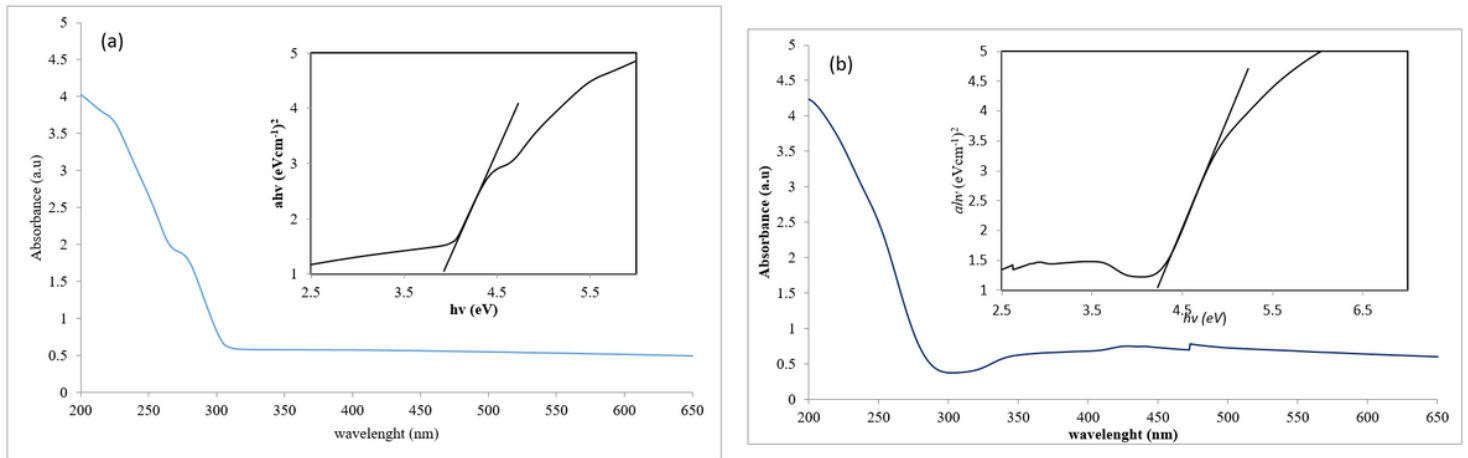


Figure 9

Absorption spectra of SnO₂ nanoparticles calcined at (a) 350 °C and (b) 600 °C. Inset show the corresponding plot of $(ah\nu)^2$ vs photon energy for the SnO₂ nanoparticles.

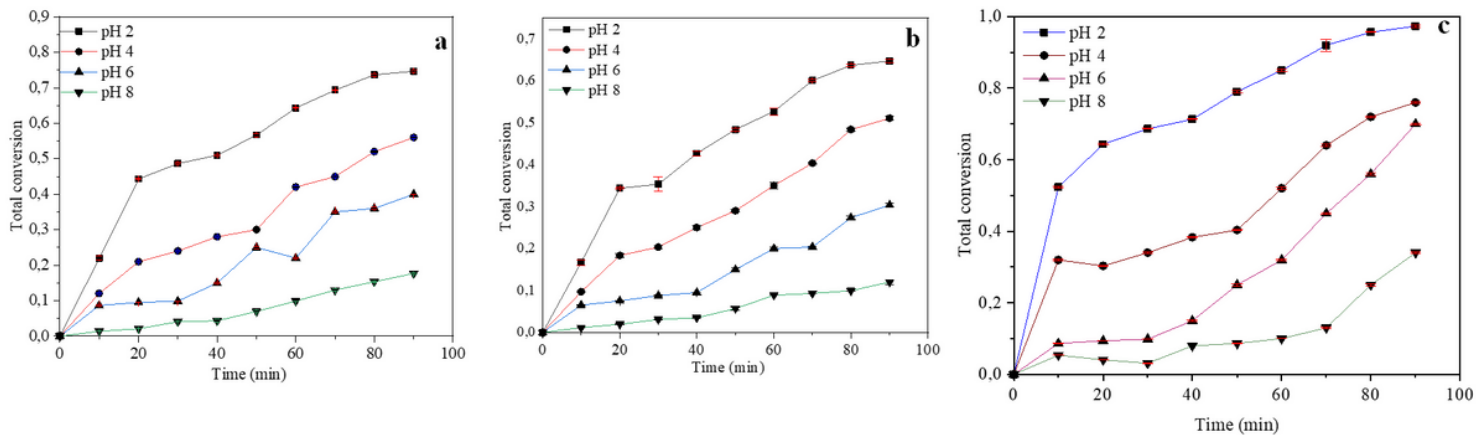


Figure 10

The effect of pH on the photo reduction of Cr(VI) on (a) ZnO (b) SnO₂ (c) ZnO-SnO₂ nanocomposite synthesised using bio-surfactants from extract of *Solanum macrocarpon*

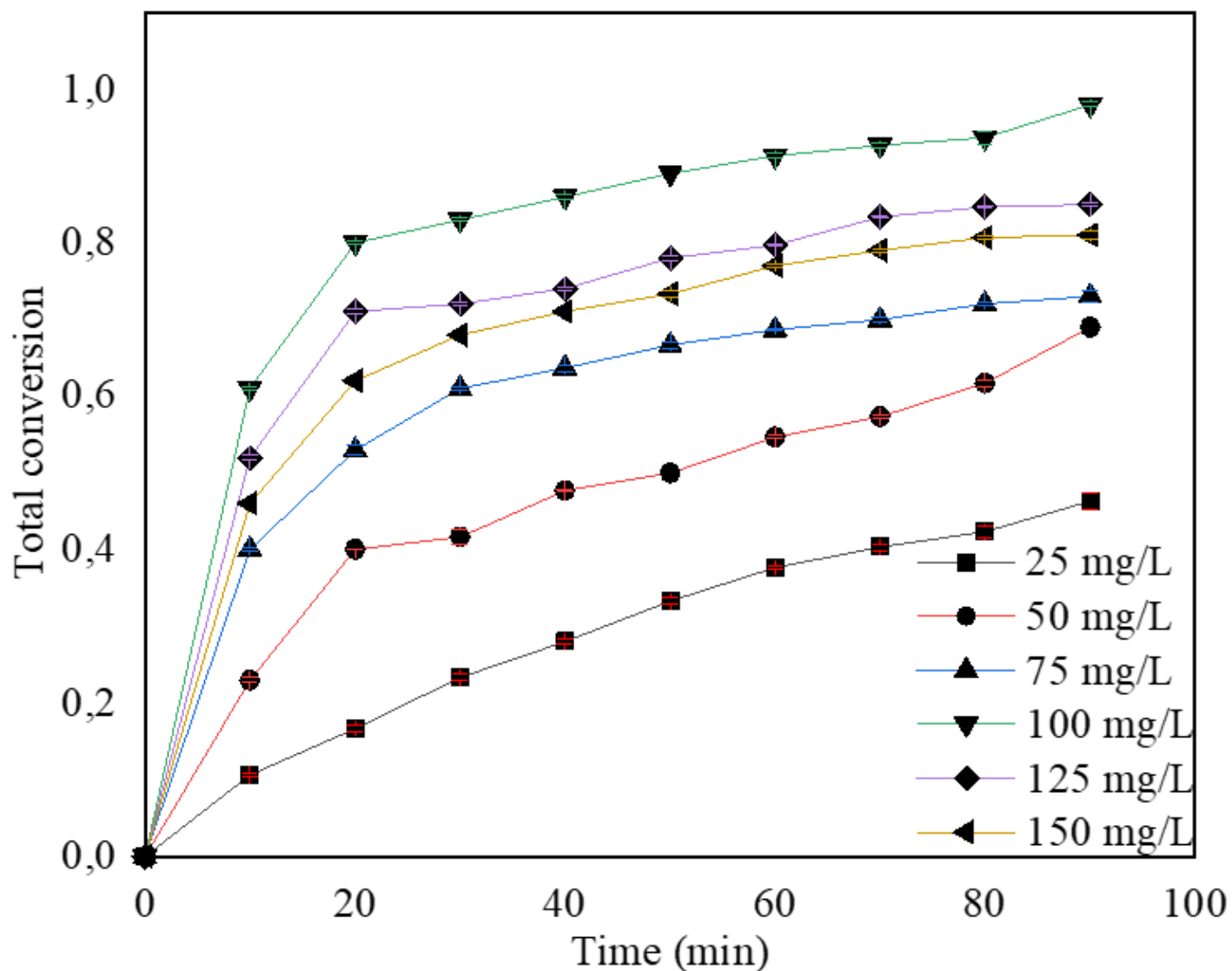


Figure 11

The effect of catalyst loading on the photoreduction of Cr(VI) on to ZnO-SnO₂ nanocomposite.

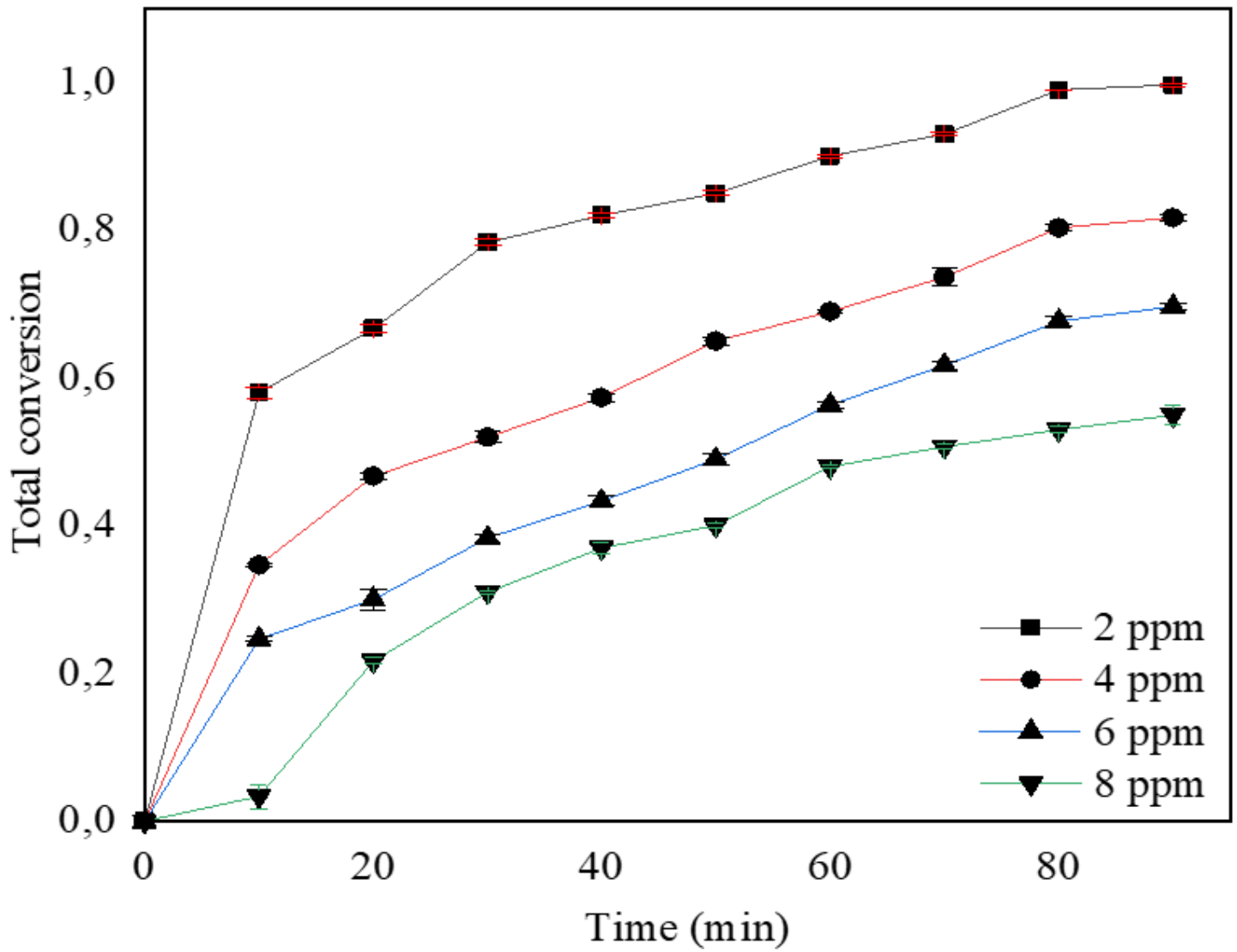


Figure 12

The effect of initial concentration of Cr(VI) on photoreduction using ZnO-SnO₂ nanocomposite.

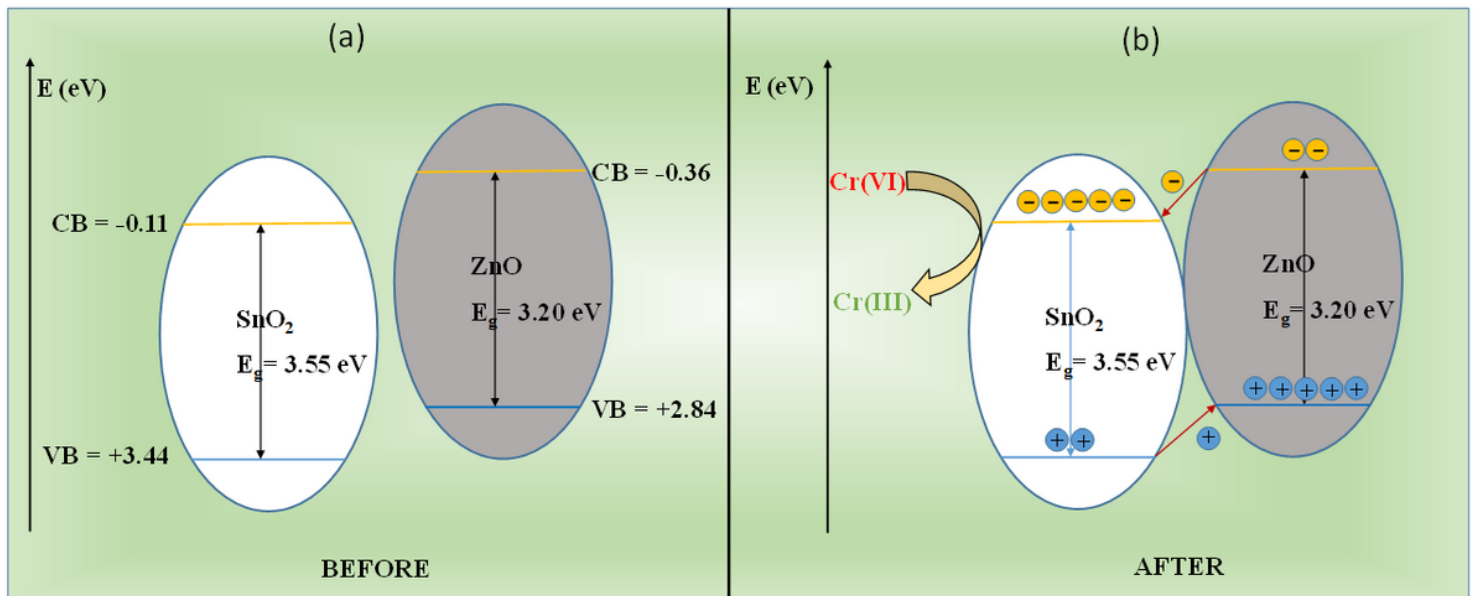


Figure 13

Schematic presentation of the band structure and e⁻-h⁺ separation in the ZnO and SnO₂ before and after compositing